Report

Current Biology

Microtubule End-Clustering Maintains a Steady-State Spindle Shape

Graphical Abstract

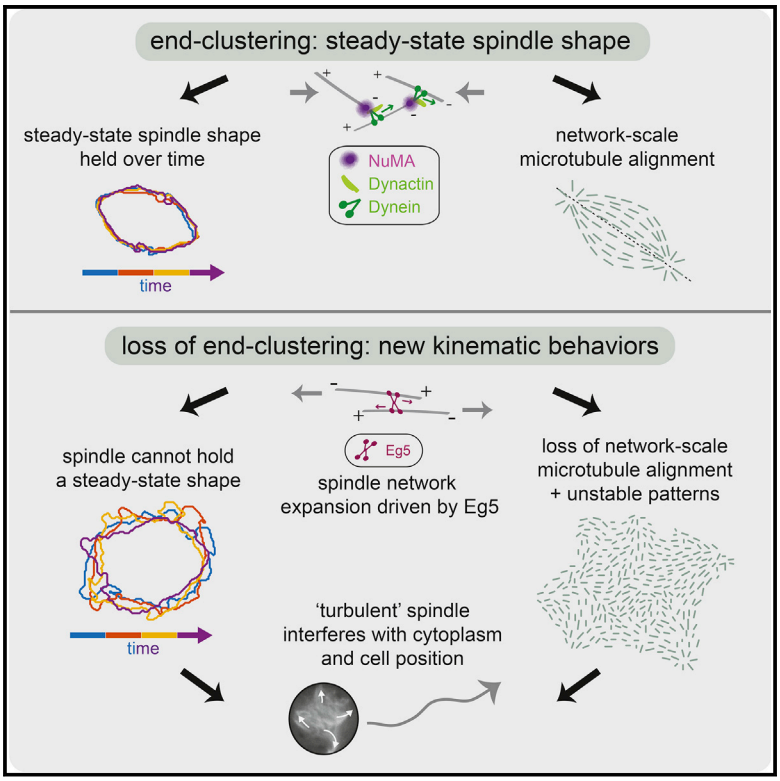

Highlights

- Mammalian spindles use microtubule end-clustering by dynein or NuMA to hold their shape
- Dynein or NuMA knockout spindles are unstable and turbulent
- The kinesin Eg5 expands turbulent spindle networks and drives shape change
- Turbulent spindles reorganize cytoplasm and increase cell movement

Authors

Christina L. Hueschen, Vahe Galstyan, Meelad Amouzgar, Rob Phillips, Sophie Dumont

Correspondence

chueschen@gmail.com (C.L.H.), sophie.dumont@ucsf.edu (S.D.)

In Brief

Hueschen et al. show that mitotic spindles use clustering of microtubule ends by the motor dynein to maintain a steady-state spindle network shape. After complete loss of dynein or its partner NuMA, spindles dynamically remodel their shape and microtubule organization, and these unstable turbulent spindles can drive cell movement.

Hueschen et al., 2019, Current Biology 29, 700–708
February 18, 2019
https://doi.org/10.1016/j.cub.2019.01.016

CellPress

CellPress

Current Biology
Report

Microtubule End-Clustering Maintains a Steady-State Spindle Shape

Christina L. Hueschen,[1,2,*] Vahe Galstyan,[3] Meelad Amouzgar,[1] Rob Phillips,[4,5] and Sophie Dumont[1,2,6,7,*]
[1]Department of Cell and Tissue Biology, UCSF, San Francisco, CA 94143, USA
[2]Biomedical Sciences Graduate Program, UCSF, San Francisco, CA 94143, USA
[3]Biochemistry and Molecular Biophysics Option, California Institute of Technology, Pasadena, CA 91106, USA
[4]Department of Physics, California Institute of Technology, Pasadena, CA 91106, USA
[5]Division of Biology and Biological Engineering, California Institute of Technology, Pasadena, CA 91106, USA
[6]Department of Cellular and Molecular Pharmacology, UCSF, San Francisco, CA 94143, USA
[7]Lead Contact
*Correspondence: chueschen@gmail.com (C.L.H.), sophie.dumont@ucsf.edu (S.D.)
https://doi.org/10.1016/j.cub.2019.01.016

SUMMARY

Each time a cell divides, the microtubule cytoskeleton self-organizes into the metaphase spindle: an ellipsoidal steady-state structure that holds its stereotyped geometry despite microtubule turnover and internal stresses [1–6]. Regulation of microtubule dynamics, motor proteins, microtubule crosslinking, and chromatid cohesion can modulate spindle size and shape, and yet modulated spindles reach and hold a new steady state [7–11]. Here, we ask what maintains any spindle steady-state geometry. We report that clustering of microtubule ends by dynein and NuMA is essential for mammalian spindles to hold a steady-state shape. After dynein or NuMA deletion, the mitotic microtubule network is "turbulent"; microtubule bundles extend and bend against the cell cortex, constantly remodeling network shape. We find that spindle turbulence is driven by the homotetrameric kinesin-5 Eg5, and that acute Eg5 inhibition in turbulent spindles recovers spindle geometry and stability. Inspired by *in vitro* work on active turbulent gels of microtubules and kinesin [12, 13], we explore the kinematics of this *in vivo* turbulent network. We find that turbulent spindles display decreased nematic order and that motile asters distort the nematic director field. Finally, we see that turbulent spindles can drive both flow of cytoplasmic organelles and whole-cell movement—analogous to the autonomous motility displayed by droplet-encapsulated turbulent gels [12]. Thus, end-clustering by dynein and NuMA is required for mammalian spindles to reach a steady-state geometry, and in their absence Eg5 powers a turbulent microtubule network inside mitotic cells.

RESULTS AND DISCUSSION

End-Clustering by Dynein and NuMA Is Required for a Steady-State Spindle Geometry

Microtubule end-clustering by motors generates contractile stresses that compact isotropic microtubule networks to a defined geometry *in vitro* and *in silico* [14–20]. In mammalian cells, the dynein-dynactin-NuMA complex robustly clusters microtubule ends at mitosis (Figure 1A) [21, 22]; NuMA is released from the nucleus upon mitotic entry and localizes to minus-ends, recruiting dynein activity there [23]. Thus, we hypothesized that in addition to its role in shaping focused spindle poles [24–27], the dynein-dynactin-NuMA complex compacts the spindle microtubule network to a defined steady-state geometry, which holds its shape over time. To test this hypothesis, we deleted dynein or NuMA using an inducible CRISPR-Cas9 system in human RPE1 cell lines (Figures S1A and S1B). Strikingly, in mitotic cells in which dynein or NuMA was deleted, spindles failed to reach a steady-state geometry (Figures 1B and 1C; Videos S1, S2, and S3). Instead, the microtubule network was dynamic and disordered; asters and microtubule bundles extended in unpredictable directions before bending against the cell cortex (Figure S1C). Centriole pairs were frequently split, and spindles contained an average of ~5 microtubule asters (Figures S1D–S1F). Cells remained in mitosis for hours, unable to enter anaphase, without reaching any spindle steady-state shape. Knockout spindles were larger in size than control spindles and explored a broad space of shape configurations (Figures 1C, 1D, and S1G–S1J), indicating that dynein and NuMA are both required for the spindle to reach a steady-state geometry. That dynein is essential reveals a requirement for active force generation, and that NuMA is essential reveals a requirement for minus-end-localized force [23]; we conclude therefore that minus-end-clustering is key to holding spindle shape at a deterministic steady state.

The irregular, disordered spindle motion and dynamic changes in spindle organization observed after dynein or NuMA knockout are reminiscent of turbulent active nematic materials [12, 28]. Henceforth, we use the term turbulent to refer to these unstable, constantly remodeling dynein or NuMA knockout

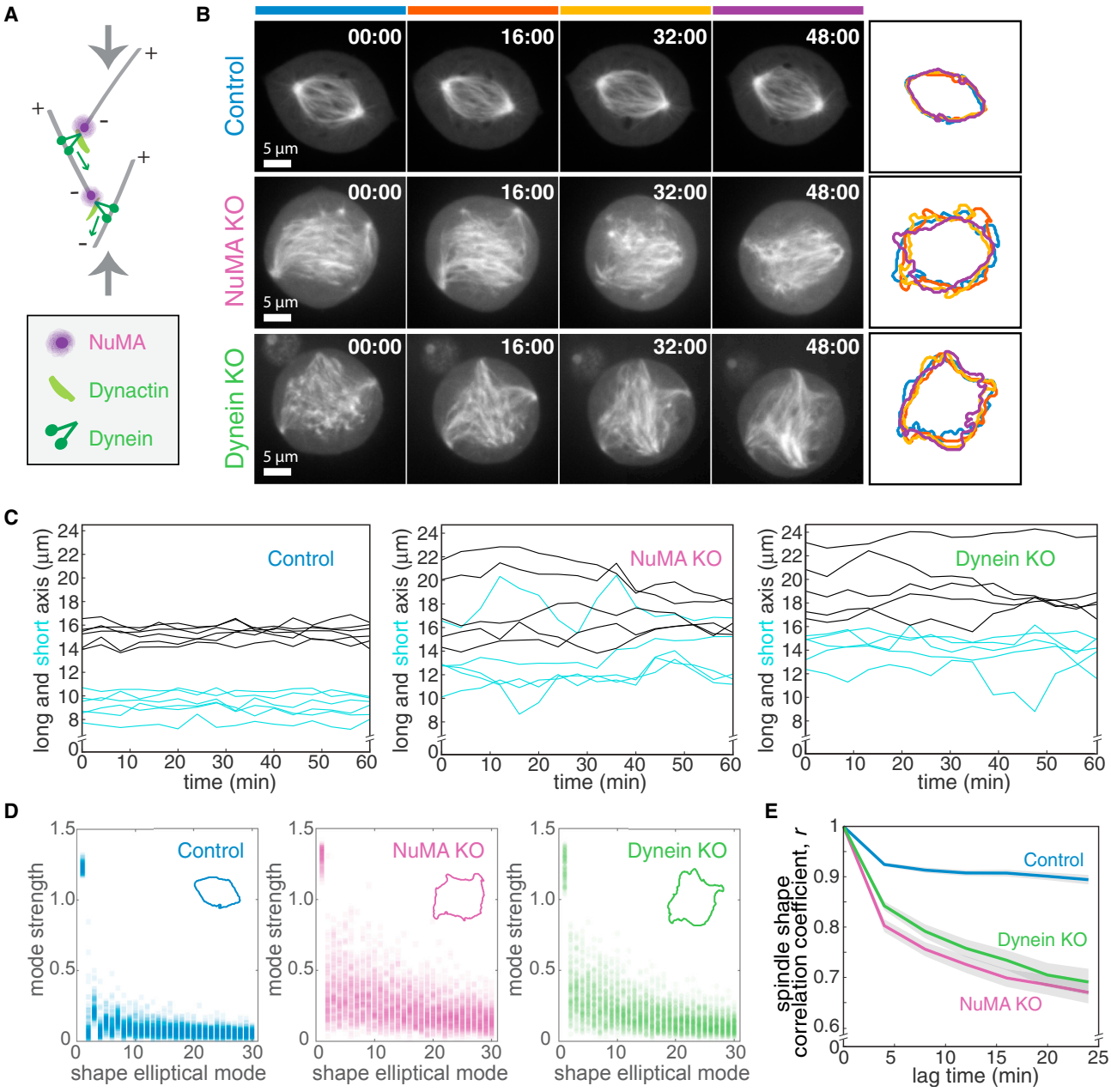

Figure 1. End-Clustering by Dynein and NuMA Is Required for a Steady-State Spindle Geometry

(A) Schematic of microtubule minus-end-clustering by the dynein-dynactin-NuMA complex. End-clustering can generate contractile stresses (large arrows) that compact microtubule networks [14–20].

(B) Time-lapse live images of spindles in RPE1 cells stably expressing GFP-tubulin. Time is in min:s. Right panel shows spindle network outlines, with position always aligned to cell centroid. Colors correspond to times indicated by bars above time-lapse image. Control spindles (held at metaphase with 5 μM MG132) maintain a steady-state geometry, while spindles in which NuMA or dynein has been knocked out (KO) constantly remodel their shapes.

(C) Representative examples of spindle long- and short-axis dimensions (see STAR Methods) over time (n = 5–6 example cells for each condition).

(D) Quantification of spindle shape by elliptical Fourier analysis (see STAR Methods). Control spindles show a consistent and restricted shape profile, while KO spindle shape profiles are complex and heterogeneous.

(E) Mean and SEM (gray shading) of spindle shape correlation coefficient (see STAR Methods) comparing two frames from binary, segmented videos of spindles, as a function of the time interval between those frames (lag time). For turbulent (dynein and NuMA KO) spindles, correlation decays exponentially with a mean lifetime of ~5–7 min (see Figure S1K) (n = 10 cells each condition).

See also Figure S1 and Videos S1, S2, and S3.

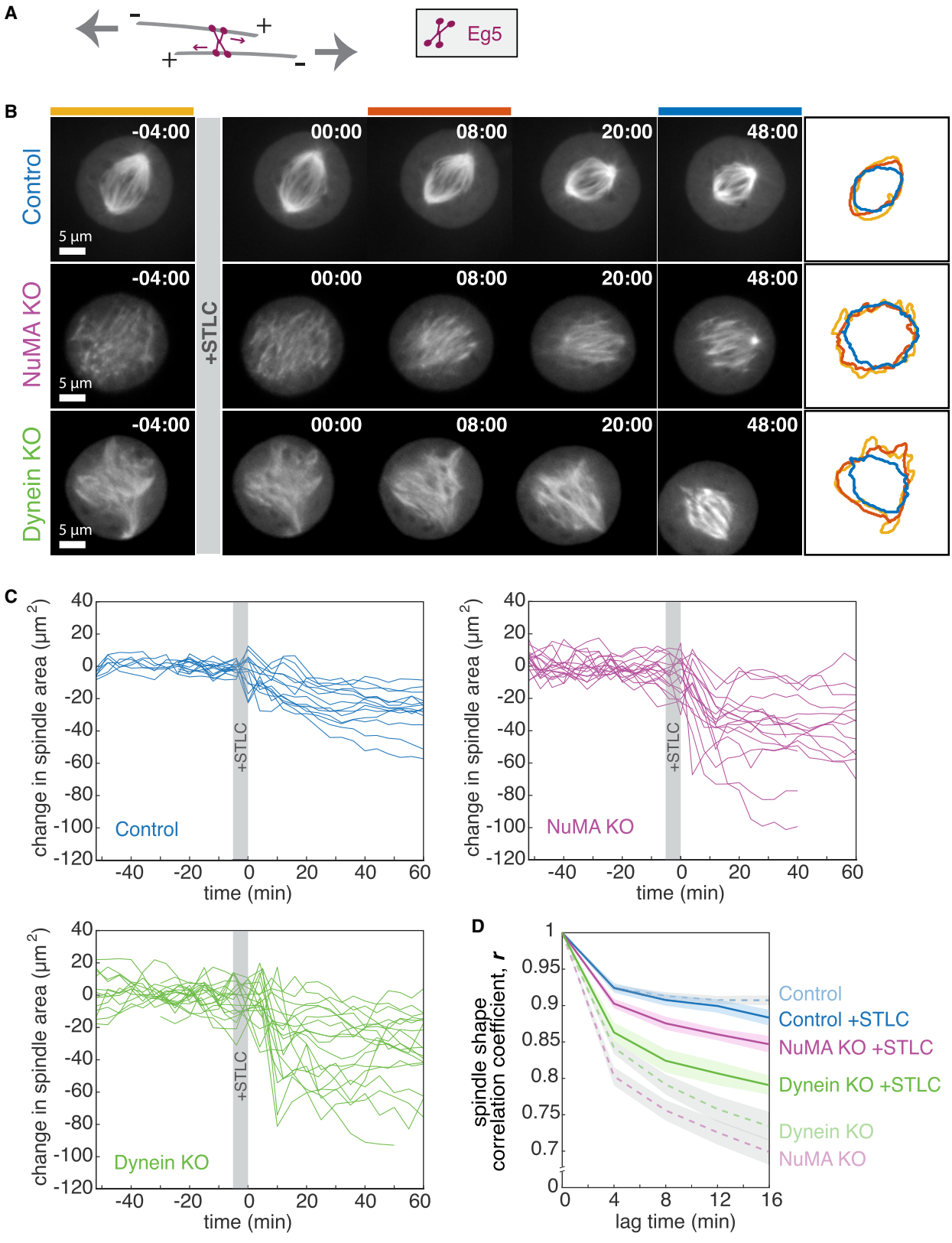

(legend on next page)

spindles. To estimate the timescale of turbulent spindle remodeling, we sought to quantify shape change as a function of time. As a simple metric of spindle geometry similarity, we calculated a correlation coefficient between two binary images of the same segmented spindle (at times t_1 and t_2), capturing the degree of shape overlap. In the absence of end-clustering, this spindle shape correlation decayed exponentially as the time interval (lag time) between t_1 and t_2 increased, with a decay lifetime of ~5–7 min (Figures 1E and S1K). This timescale of network remodeling, or "spindle shape memory," is shorter than the spindle lifetime required to accomplish chromosome segregation (20–30 min in RPE1 cells [29, 30]). By contrast, in control spindles, spindle geometry remained correlated over longer times (Figure 1E). End-clustering appeared to act as a homeostatic "restoring force" that pushed spindles back to a steady-state shape. Thus, clustering of microtubule ends by dynein and NuMA compacts the spindle microtubule network and suppresses network turbulence, maintaining a steady-state spindle geometry over long timescales.

In the Absence of Dynein or NuMA, Eg5 Drives Spindle Expansion and Turbulent Microtubule Motion

We next sought to determine what active mechanism drove the spindle turbulence observed in the absence of dynein or NuMA. The bipolar homotetrameric kinesin-5 Eg5 can slide overlapping antiparallel microtubules apart (Figure 2A) [31–34] but does not resist large-scale contraction of an isotropic microtubule network in meiotic extract [16], indicating that Eg5 sliding events may not translate into long-range expansion in an isotropic network. Given the local microtubule alignment present in spindles, however, we wondered whether Eg5 could drive network expansion in this context.

Indeed, Eg5 inhibition using 5 μM *S*-trityl-l-cysteine (STLC) [35] decreased spindle turbulence as well as bundle and aster extensions upon acute addition to dynein and NuMA knockout cells (Figure 2B; Video S4). Spindle size in knockout cells decreased strikingly after Eg5 inhibition, and within 10–20 min spindles remodeled to a size and geometry more similar to a wild-type metaphase steady state (Figures 2B and 2C; Video S4). To quantify spindle dynamics after Eg5 inhibition, we calculated spindle shape correlation (spindle shape overlap) as a function of the time interval between images, as in Figure 1E. After Eg5 inhibition, dynein and NuMA knockout spindles remained more correlated over time and more similar to control spindles (Figure 2D). Thus, the data indicate that Eg5 drives turbulent kinematics and expansion of the mitotic microtubule network in the absence of microtubule end-clustering (and network compaction) by dynein and NuMA. Interestingly, the network turbulence we observe displays similarities to turbulence observed in active matter systems consisting of purified microtubules and driven by artificially multimerized kinesin-1 [12, 13, 36]. We note with excitement that the naturally homotetrameric kinesin Eg5 can drive analogous dynamics *in vivo*.

Turbulent Spindles Display Topological Defects and Decreased Nematic Order

Next, we sought to investigate the local and global organization and the kinematics of a turbulent, kinesin-driven microtubule network. To enable whole-network imaging and to simplify networks to roughly two dimensions, we physically confined control and NuMA knockout mitotic cells in polydimethylsiloxane (PDMS) devices [37]. Turbulent spindles remained highly dynamic and disordered (Figure 3A), and we observed multiple small, motile asters (Figures 1A and 3A) that frequently repelled each other. The repulsion of overlapping asters, which are polar arrays with minus-ends anchored at their cores (Figure S1D), is consistent with Eg5-powered extension of antiparallel microtubule overlaps within a disordered network. Again, these Eg5-driven dynamics were reminiscent of turbulent, extensile *in vitro* active matter systems, which contain microtubules bundled by a depletion agent and are driven by artificially multimerized kinesin-1 [12]. An active liquid crystal framework has provided quantitative insight into those *in vitro* experiments, which have been described as active nematic systems: "active" because motors convert ATP into motion, and "nematic" because their constituent particles, microtubules, are aligned. In those systems, continual active extension of microtubule bundles by kinesin leads to larger scale turbulence, loss of microtubule alignment (nematic order), and motile topological defects [12, 13].

To explore whether the active nematic framework and associated kinematic descriptions might apply in our *in vivo* setting, we extracted the nematic director field (a map of microtubule orientations) from fluorescence images (Figures 3B and S2A–S2C). While control spindles show two topological defects in the director field (at spindle poles), turbulent spindles contain defects throughout the whole network (Figure 3B). In turbulent spindles, aster "defects" moved along unpredictable trajectories (Figure S2D), and their movement distorted and reordered the director field (Figure 3B, zoom). At a local scale (<2 μm), control and turbulent spindles showed similarly high nematic order (Figures 3C, 3D, S2E, and S2F). Since functional chromosome segregation involves microtubule alignment at the whole-network scale, we also calculated a global nematic order parameter for each spindle (Figure 3E). Turbulent spindles displayed decreased nematic order at this whole-network scale; the mean global

Figure 2. Eg5 Drives Spindle Expansion and Turbulence

(A) Schematic of outward microtubule sliding by the homotetrameric kinesin Eg5.

(B) Time-lapse live images of spindles in RPE1 cells stably expressing GFP-tubulin. Time is in min:s. Right panel shows spindle network outlines, with position always aligned to cell centroid. Time 00:00 indicates first frame after addition of 5 μM STLC to inhibit Eg5. Colors correspond to times indicated by bars above time-lapse images.

(C) Area of spindle microtubule network, relative to the mean area before STLC addition (see STAR Methods). n = 14,17,19 cells for control, NuMA knockout, and dynein knockout, respectively.

(D) Mean and SEM (shading) of correlation coefficient comparing two frames from binary, segmented videos of spindles, as a function of the time interval between those frames. Lines with colored shading show correlations from cells treated with STLC; videos used for analysis began 24 min after STLC addition. As a reference, the dashed lines with gray shading show correlations without STLC from Figure 1E.

See also Video S4.

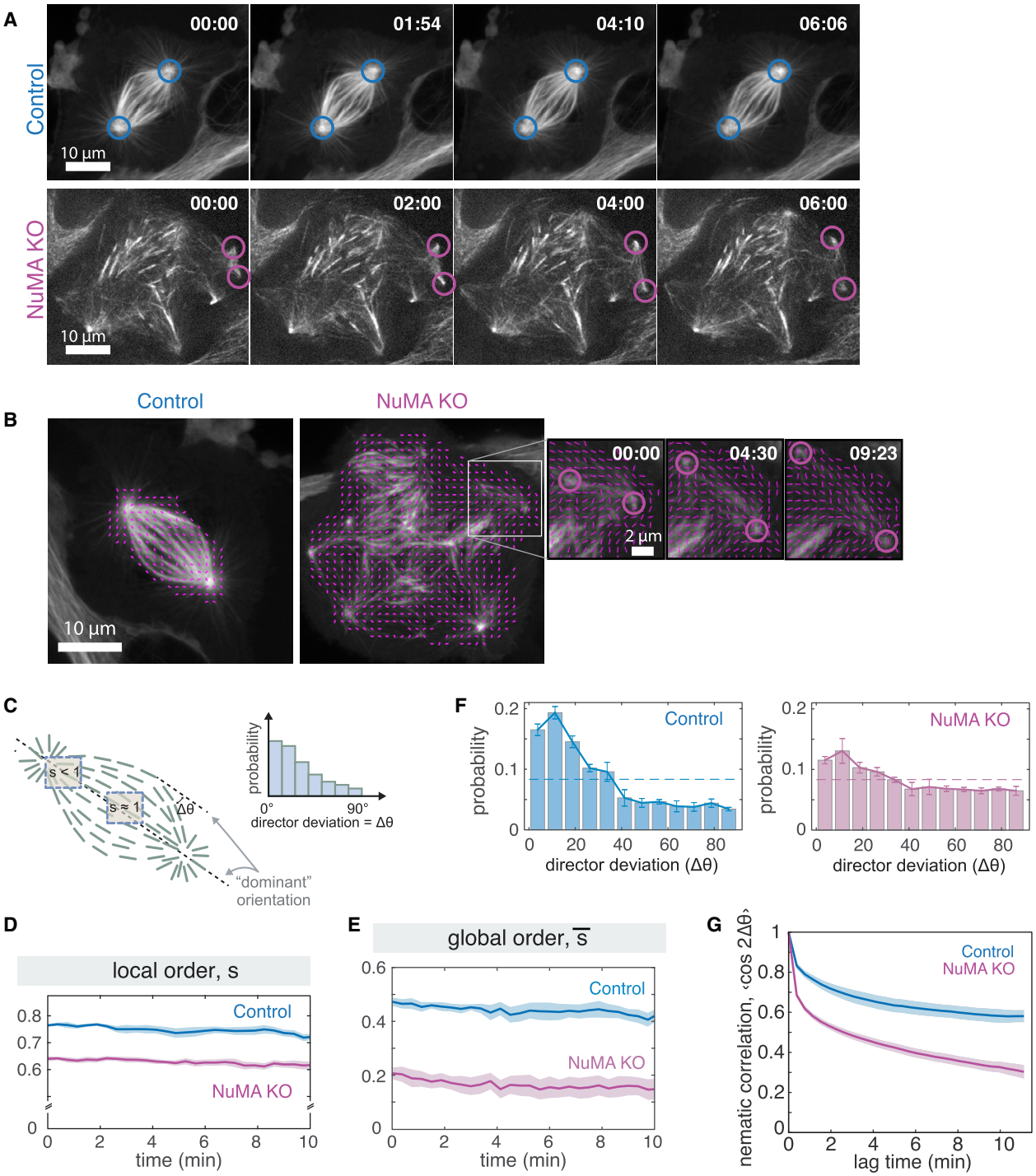

Figure 3. Turbulent Spindles Have Lower Global Nematic Order and Unstable Microtubule Organization

(A) Time-lapse live images of spindles in RPE1 cells confined in PDMS devices to allow imaging of the entire microtubule network. Time is in min:s. Circles highlight example asters, which are fixed in place in control spindles but move and repel each other in turbulent networks.

(B) Example images of nematic director fields for control and NuMA knockout spindles. Right, example of aster repulsion and motility, which dynamically distorts the director field.

(C) Schematic illustration of methods used to quantify the local and global microtubule order. The nematic order parameter, s, captures the degree of microtubule alignment. Distributions of director angles show microtubule orientation relative to the dominant spindle orientation (see Figure S2 and STAR Methods).

(D) Time dependence of the mean local nematic order parameter (evaluated over 2 × 2 μm regions).

(E) Time dependence of the mean global nematic order parameter (evaluated at the scale of the whole spindle).

(legend continued on next page)

nematic order parameter was half that of control spindles, in which most microtubules are within 25° of one dominant orientation (Figures 3E, 3F, S2E, and S2F). Factors promoting microtubule alignment, like microtubule crosslinking proteins, may maintain local order but require end-clustering by dynein and NuMA to create global alignment of locally ordered domains. Notably, while turbulent spindles are not at a deterministic steady state—the orientation of microtubules in any given region of the spindle is not fixed in time—the degree of nematic order in both control and turbulent spindles fluctuated around a statistical steady state (Figures 3D and 3E). Finally, we found that microtubule orientation was less correlated over space (Figures S2G and S2H) and time (Figure 3G) in turbulent spindles. In other words, NuMA knockout spindles showed unstable patterns of microtubule organization (Figure 3G), supporting the hypothesis that end-clustering is required for the spindle to hold a steady-state geometry. In summary, NuMA knockout spindles contain motile asters and display decreased global nematic order and temporally unstable nematic patterns, consistent with the idea that they are a turbulent material "stirred up" by active kinesin-generated stresses.

In the absence of microtubule network alignment and compaction by microtubule end-clustering, spindle turbulence may arise from (1) the motility of a multiple γ-tubulin-containing microtubule asters (Figures 3 and S1D–S1F), which distort global nematic organization and nucleate microtubules in unregulated positions and orientations, and (2) microtubule bending and buckling against the cell cortex during unchecked Eg5 bundle extension events (Figures 1, 2, and S1C). Consistent with a key contribution from the latter, dynamic spindle shape changes have not been reported after dynein inhibition in acentrosomal spindles in *Xenopus laevis* extract, which lack the physical boundary of a cell cortex and membrane [26].

Turbulent Spindles Can Drive Cytoplasmic Flow and Reorganize Cytoplasmic Organelles

Thus far, the data indicate that end-clustering by dynein and NuMA masks a disordered, unstable turbulent microtubule network. In the absence of end-clustering, spindles show altered network kinematics (e.g., dynamic geometry (Figures 1B–1D) and dynamic distortions in nematic alignment (Figures 3B and 3G) driven by the kinesin Eg5 (Figure 2)). Interestingly, we also noticed that turbulent dynein or NuMA knockout spindles reorganized cytoplasmic organelles, confining mitochondria (Figure 4A) and lysosomes (data not shown) to the periphery of the cell. In addition, we observed unusual flows of cytoplasmic organelles in mitotic knockout cells, but not in control cells (Figure 4B). These were especially clear in rare instances when dynein or NuMA knockout spindles underwent coherent whole-network rotations (Video S5), which resemble spontaneous rotations reported for dynein-inhibited meiotic microtubule networks encapsulated in droplets [39]. Indeed, particle image velocimetry (PIV) analysis during rotational flows revealed spatially coordinated microtubule flows and organelle flows (Figure 4B), suggesting that dynamic knockout spindles can drive cytoplasmic flows. In other words, the data indicate that contractile end-clustering by dynein and NuMA maintains a compact steady-state spindle geometry that is mechanically isolated from the rest of the cell. In the absence of end-clustering, extra-spindle cytoplasm and organelles are no longer isolated from spindle kinematics and forces, allowing turbulent spindles to displace organelles and generate cytoplasmic flows.

Turbulent Spindles Can Change Extracellular Mechanics, Increasing Cell Movement at Mitosis

To our surprise we noticed that, in addition to increased cytoplasmic (intracellular) dynamics, mitotic cells containing turbulent spindles appeared to display increased cell motility, sometimes moving long distances (tens of microns) when plated on coverslips at low density. To carefully compare the motility of cells containing turbulent spindles to cells containing steady-state, mechanically isolated spindles, we synchronized cells at the G2/M checkpoint and imaged cells at comparable densities from 1 h until 3 h after release into mitosis.

Indeed, cells containing turbulent spindles (NuMA knockout) showed longer, directional displacements than cells containing steady-state spindles (control cells held at metaphase with MG132) (Figure 4C; Video S6). When Eg5 was inhibited with 5 μM STLC prior to imaging to reduce spindle turbulence, cell displacement was reduced, indicating that turbulent spindle dynamics—not loss of NuMA function directly—affects cell motility (Figure 4C; Video S6). In particular, a subpopulation of cells containing turbulent spindles displayed highly directional motion (Figure 4D) compared to control cells or NuMA knockout cells treated with STLC. Importantly, the cells that underwent the largest directional displacements were those containing the most turbulent spindles: variance in cell displacement correlated with variance in orientation of the major spindle axis, a simple indicator of unstable microtubule organization (Figure 4E). We conclude that at mitosis, a steady-state spindle shape isolates cell position from spindle forces. In the absence of spindle mechanical isolation, intracellular dynamics driven by turbulent spindles can affect whole-cell mechanics and cell motility. Of note, flows of the actomyosin cell cortex are thought to reposition cells during early embryonic development in animals [40, 41]. It is possible that intracellular flows of microtubules can similarly be coupled through friction to the cell cortex and membrane to drive mitotic cell rolling, or that they increase the rate of cell-substrate adhesion breakage. We speculate that the establishment of a defined spindle shape and the suppression of network turbulence may be important not only for segregating chromosomes, but also for preventing physical interference with other cell functions.

In summary, we report that clustering of microtubule minus-ends by dynein and NuMA is required for the mammalian spindle to reach and hold a steady-state geometry. End-clustering may

(F) Distribution of director angles relative to the dominant spindle orientation. Dashed lines illustrate a fully isotropic distribution.
(G) Temporal nematic correlation of microtubule orientation $< \cos 2(\theta_{t2} - \theta_{t1}) >$ as a function of lag time, t_2-t_1. (θ_{t1} is the angle of a given director at time t_1.) (D)–(G) report on m > 200 video frames from n = 6 cells each condition. Mean traces are shown; shading indicates SEM.
See also Figure S2.

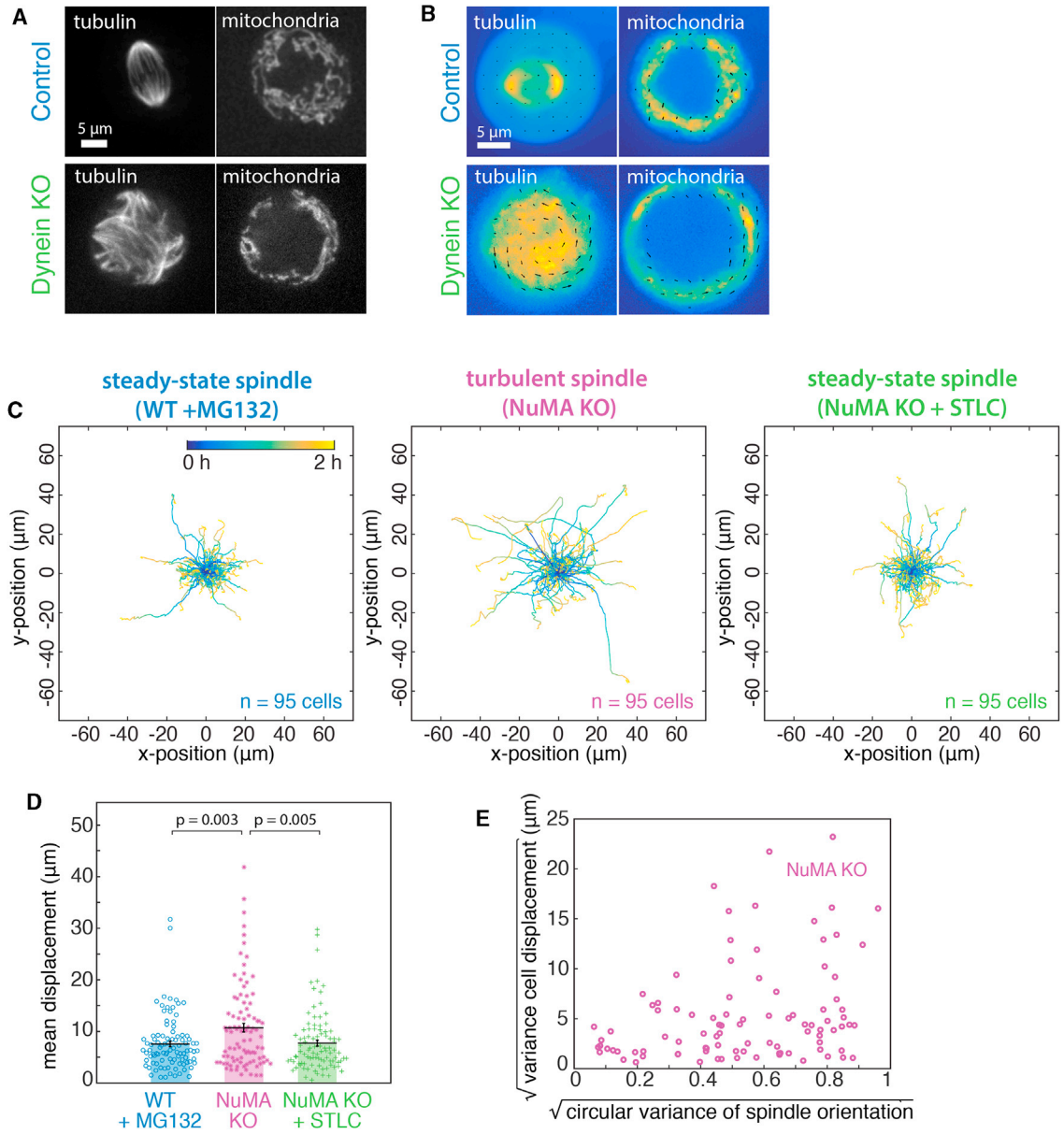

Figure 4. A Turbulent Microtubule Network Can Drive Cytoplasmic Flow and Cell Motility at Mitosis

(A) Representative images of spindles and mitochondria in live cells, labeled by GFP-tubulin and MitoTracker.

(B) Example PIV analysis of the movement of microtubules and mitochondria in cells with control and turbulent (dynein KO) spindles. Blue-to-yellow color scale shows increasing fluorescence intensity and black arrows indicate velocity, both averaged over 110 min.

(C) Tracks of cell position over a 2 h window, starting 1 h after entry into mitosis. Track color indicates time.

(D) Mean displacement from starting position. Each data point represents one cell, and black bars are mean ± SEM p values were calculated using a one-way ANOVA and Tukey post hoc test.

(E) Scatterplot showing a correlation between cell motility (represented by the square root of the variance of cell displacement) and spindle turbulence (represented by the square root of the circular variance [38] of the dominant spindle orientation angle). Spearman's rank correlation coefficient = 0.2, p = 0.01. n = 95 cells for each condition.

See also Videos S5 and S6.

limit spindle size and geometry by generating contractile stresses that compact the microtubule network, as observed for isotropic microtubule networks *in vitro* and *in silico* [14–20]. In the absence of end-clustering, the homotetrameric kinesin Eg5 can expand the mitotic microtubule network and drive it into a turbulent state of decreased nematic order, which resembles turbulent active nematic gels comprising purified microtubule bundles and kinesin [12]. Interestingly, when those turbulent gels were encapsulated in emulsion droplets, droplets exhibited persistent autonomous motility [12]. Here, we find that turbulent

spindles can drive cytoplasmic flows and persistent cell movement—an *in vivo* example of this physical mechanism.

STAR★METHODS

Detailed methods are provided in the online version of this paper and include the following:

- KEY RESOURCES TABLE
- CONTACT FOR REAGENT AND RESOURCE SHARING
- EXPERIMENTAL MODEL AND SUBJECT DETAILS
- METHOD DETAILS
  - Live cell imaging
  - Immunofluorescence and antibodies
  - Small molecule treatment
  - Cell confinement
- QUANTIFICATION AND STATISTICAL ANALYSIS
  - Quantification of spindle shape
  - Elliptical Fourier analysis of spindle shapes
  - Time correlation function of spindle shape
  - Nematic director field, order parameter, and correlation function
  - Tracking aster dynamics
  - Measuring intracellular flows and cell motility
  - Quantification of NuMA and dynein immunofluorescence
  - Statistical analysis

SUPPLEMENTAL INFORMATION

Supplemental Information includes two figures and six videos and can be found with this article online at https://doi.org/10.1016/j.cub.2019.01.016.

ACKNOWLEDGMENTS

We thank Andrea Serra-Marques and Josh Guild for experimental assistance and advice, Iain Cheeseman and Kara McKinley for key reagents and advice, Nigel Orme for Figure S2H visualization, and Justin Bois, Jan Brugués, Zvonimir Dogic, Sebastien Fürthauer, Mike Hagan, Jané Kondev, Dan Needleman, the Fred Chang Lab, and the Dumont Lab for wonderful discussions. Special thanks to the Marine Biological Laboratory Physiology course and MBL post-course research support from the Burroughs Wellcome Fund. This work was supported by NIH DP2GM119177 (S.D.), the Searle Scholars Program and Rita Allen Scholars Program (S.D.), NSF 1548297 to the Center for Cellular Construction (S.D.), an NIH NRSA F31 (C.L.H.), the UCSF Moritz Heyman Discovery Fellowship (C.L.H.), NIH 1R35 GM118043-01 (R.P.), and the John Templeton Foundation as part of the Boundaries of Life Initiative grants 51250 and 60973 (R.P.).

AUTHOR CONTRIBUTIONS

Conceptualization, C.L.H., R.P., and S.D.; Investigation, C.L.H. and M.A.; Formal Analysis – C.L.H. and V.G.; Visualization – C.L.H. and V.G.; Writing – Original Draft, C.L.H.; Writing – Review & Editing, C.L.H., V.G., R.P., and S.D.; Funding Acquisition, C.L.H., R.P., and S.D.; Supervision, R.P. and S.D.

DECLARATION OF INTERESTS

The authors declare no competing interests.

Received: July 26, 2018
Revised: November 26, 2018
Accepted: January 8, 2019
Published: February 7, 2019

REFERENCES

1. Saxton, W.M., Stemple, D.L., Leslie, R.J., Salmon, E.D., Zavortink, M., and McIntosh, J.R. (1984). Tubulin dynamics in cultured mammalian cells. J. Cell Biol. *99*, 2175–2186.
2. Gorbsky, G.J., Simerly, C., Schatten, G., and Borisy, G.G. (1990). Microtubules in the metaphase-arrested mouse oocyte turn over rapidly. Proc. Natl. Acad. Sci. USA *87*, 6049–6053.
3. Dumont, S., and Mitchison, T.J. (2009). Force and length in the mitotic spindle. Curr. Biol. *19*, R749–R761.
4. McIntosh, J.R., Molodtsov, M.I., and Ataullakhanov, F.I. (2012). Biophysics of mitosis. Q. Rev. Biophys. *45*, 147–207.
5. Brugués, J., and Needleman, D. (2014). Physical basis of spindle self-organization. Proc. Natl. Acad. Sci. USA *111*, 18496–18500.
6. Oriola, D., Needleman, D.J., and Brugués, J. (2018). The physics of the metaphase spindle. Annu. Rev. Biophys. *47*, 655–673.
7. Goshima, G., Wollman, R., Stuurman, N., Scholey, J.M., and Vale, R.D. (2005). Length control of the metaphase spindle. Curr. Biol. *15*, 1979–1988.
8. Goshima, G., and Scholey, J.M. (2010). Control of mitotic spindle length. Annu. Rev. Cell Dev. Biol. *26*, 21–57.
9. Helmke, K.J., Heald, R., and Wilbur, J.D. (2013). Interplay between spindle architecture and function. Int. Rev. Cell Mol. Biol. *306*, 83–125.
10. Crowder, M.E., Strzelecka, M., Wilbur, J.D., Good, M.C., von Dassow, G., and Heald, R. (2015). A comparative analysis of spindle morphometrics across metazoans. Curr. Biol. *25*, 1542–1550.
11. Farhadifar, R., Baer, C.F., Valfort, A.C., Andersen, E.C., Müller-Reichert, T., Delattre, M., and Needleman, D.J. (2015). Scaling, selection, and evolutionary dynamics of the mitotic spindle. Curr. Biol. *25*, 732–740.
12. Sanchez, T., Chen, D.T.N., DeCamp, S.J., Heymann, M., and Dogic, Z. (2012). Spontaneous motion in hierarchically assembled active matter. Nature *491*, 431–434.
13. DeCamp, S.J., Redner, G.S., Baskaran, A., Hagan, M.F., and Dogic, Z. (2015). Orientational order of motile defects in active nematics. Nat. Mater. *14*, 1110–1115.
14. Surrey, T., Nedelec, F., Leibler, S., and Karsenti, E. (2001). Physical properties determining self-organization of motors and microtubules. Science *292*, 1167–1171.
15. Burbank, K.S., Mitchison, T.J., and Fisher, D.S. (2007). Slide-and-cluster models for spindle assembly. Curr. Biol. *17*, 1373–1383.
16. Foster, P.J., Fürthauer, S., Shelley, M.J., and Needleman, D.J. (2015). Active contraction of microtubule networks. eLife *4*. Published online December 23, 2015. https://doi.org/10.7554/eLife.10837.
17. Torisawa, T., Taniguchi, D., Ishihara, S., and Oiwa, K. (2016). Spontaneous formation of a globally connected contractile network in a microtubule-motor system. Biophys. J. *111*, 373–385.
18. Belmonte, J.M., Leptin, M., and Nédélec, F. (2017). A theory that predicts behaviors of disordered cytoskeletal networks. Mol. Syst. Biol. *13*, 941.
19. Tan, R., Foster, P.J., Needleman, D.J., and McKenney, R.J. (2018). Cooperative accumulation of dynein-dynactin at microtubule minus-ends drives microtubule network reorganization. Dev. Cell *44*, 233–247.
20. Roostalu, J., Rickman, J., Thomas, C., Nedelec, F., and Surrey, T. (2018). Determinants of polar versus nematic organization in networks of dynamic microtubules and mitotic motors. Cell *175*, 796–808.
21. Elting, M.W., Hueschen, C.L., Udy, D.B., and Dumont, S. (2014). Force on spindle microtubule minus ends moves chromosomes. J. Cell Biol. *206*, 245–256.
22. Sikirzhytski, V., Magidson, V., Steinman, J.B., He, J., Le Berre, M., Tikhonenko, I., Ault, J.G., McEwen, B.F., Chen, J.K., Sui, H., et al. (2014). Direct kinetochore-spindle pole connections are not required for chromosome segregation. J. Cell Biol. *206*, 231–243.

23. Hueschen, C.L., Kenny, S.J., Xu, K., and Dumont, S. (2017). NuMA recruits dynein activity to microtubule minus-ends at mitosis. eLife *6*. Published online November 29, 2017. https://doi.org/10.7554/eLife.29328.
24. Gaglio, T., Saredi, A., and Compton, D.A. (1995). NuMA is required for the organization of microtubules into aster-like mitotic arrays. J. Cell Biol. *131*, 693–708.
25. Merdes, A., Ramyar, K., Vechio, J.D., and Cleveland, D.W. (1996). A complex of NuMA and cytoplasmic dynein is essential for mitotic spindle assembly. Cell *87*, 447–458.
26. Heald, R., Tournebize, R., Blank, T., Sandaltzopoulos, R., Becker, P., Hyman, A., and Karsenti, E. (1996). Self-organization of microtubules into bipolar spindles around artificial chromosomes in Xenopus egg extracts. Nature *382*, 420–425.
27. Verde, F., Berrez, J.M., Antony, C., and Karsenti, E. (1991). Taxol-induced microtubule asters in mitotic extracts of Xenopus eggs: Requirement for phosphorylated factors and cytoplasmic dynein. J. Cell Biol. *112*, 1177–1187.
28. Doostmohammadi, A., Ignés-Mullol, J., Yeomans, J.M., and Sagués, F. (2018). Active nematics. Nat. Commun. *9*, 3246.
29. Uetake, Y., and Sluder, G. (2010). Prolonged prometaphase blocks daughter cell proliferation despite normal completion of mitosis. Curr. Biol. *20*, 1666–1671.
30. Yang, Z., Loncarek, J., Khodjakov, A., and Rieder, C.L. (2008). Extra centrosomes and/or chromosomes prolong mitosis in human cells. Nat. Cell Biol. *10*, 748–751.
31. Kapitein, L.C., Peterman, E.J., Kwok, B.H., Kim, J.H., Kapoor, T.M., and Schmidt, C.F. (2005). The bipolar mitotic kinesin Eg5 moves on both microtubules that it crosslinks. Nature *435*, 114–118.
32. Kapoor, T.M., Mayer, T.U., Coughlin, M.L., and Mitchison, T.J. (2000). Probing spindle assembly mechanisms with monastrol, a small molecule inhibitor of the mitotic kinesin, Eg5. J. Cell Biol. *150*, 975–988.
33. Tanenbaum, M.E., Macůrek, L., Galjart, N., and Medema, R.H. (2008). Dynein, Lis1 and CLIP-170 counteract Eg5-dependent centrosome separation during bipolar spindle assembly. EMBO J. *27*, 3235–3245.
34. Kashina, A.S., Baskin, R.J., Cole, D.G., Wedaman, K.P., Saxton, W.M., and Scholey, J.M. (1996). A bipolar kinesin. Nature *379*, 270–272.
35. Skoufias, D.A., DeBonis, S., Saoudi, Y., Lebeau, L., Crevel, I., Cross, R., Wade, R.H., Hackney, D., and Kozielski, F. (2006). S-trityl-L-cysteine is a reversible, tight binding inhibitor of the human kinesin Eg5 that specifically blocks mitotic progression. J. Biol. Chem. *281*, 17559–17569.
36. Wu, K.T., Hishamunda, J.B., Chen, D.T.N., DeCamp, S.J., Chang, Y.W., Fernandez-Nieves, A., Fraden, S., and Dogic, Z. (2017). ACTIVE MATTER Transition from turbulent to coherent flows in confined three-dimensional active fluids. Science *355*. Published online March 24, 2017. https://doi.org/10.1126/science.aal1979.
37. Guild, J., Ginzberg, M.B., Hueschen, C.L., Mitchison, T.J., and Dumont, S. (2017). Increased lateral microtubule contact at the cell cortex is sufficient to drive mammalian spindle elongation. Mol. Biol. Cell *28*, 1975–1983.
38. Berens, P. (2009). CircStat: A Matlab toolbox for circular statistics. J. Stat. Softw. Published online September 23, 2009. https://doi.org/10.18637/jss.v031.i10.
39. Suzuki, K., Miyazaki, M., Takagi, J., Itabashi, T., and Ishiwata, S. (2017). Spatial confinement of active microtubule networks induces large-scale rotational cytoplasmic flow. Proc. Natl. Acad. Sci. USA *114*, 2922–2927.
40. Gerhart, J., Danilchik, M., Doniach, T., Roberts, S., Rowning, B., and Stewart, R. (1989). Cortical rotation of the Xenopus egg: Consequences for the anteroposterior pattern of embryonic dorsal development. Development *107* (*Suppl*), 37–51.
41. Naganathan, S.R., Fürthauer, S., Nishikawa, M., Jülicher, F., and Grill, S.W. (2014). Active torque generation by the actomyosin cell cortex drives left-right symmetry breaking. eLife *3*, e04165.
42. McKinley, K.L., and Cheeseman, I.M. (2017). Large-scale analysis of CRISPR/Cas9 cell-cycle knockouts reveals the diversity of p53-dependent responses to cell-cycle defects. Dev. Cell *40*, 405–420.
43. Thielicke, W.S., E. J. (2014). Towards user-friendly, affordable and accurate digital particle image velocimetry in MATLAB. J. Open Res. Softw. 2, e30.
44. Thielicke, W.S., and Stamhuis, E.J. (2014). PIVlab—Time-resolved digital particle image velocimetry tool for MATLAB (version: 1.41). (figshare.com archive) https://figshare.com/articles/PIVlab_version_1_35/1092508.
45. Tinevez, J.Y., Perry, N., Schindelin, J., Hoopes, G.M., Reynolds, G.D., Laplantine, E., Bednarek, S.Y., Shorte, S.L., and Eliceiri, K.W. (2017). TrackMate: An open and extensible platform for single-particle tracking. Methods *115*, 80–90.
46. McKinley, K.L., Sekulic, N., Guo, L.Y., Tsinman, T., Black, B.E., and Cheeseman, I.M. (2015). The CENP-L-N complex forms a critical node in an integrated meshwork of interactions at the centromere-kinetochore interface. Mol. Cell *60*, 886–898.
47. Wang, G., McCain, M.L., Yang, L., He, A., Pasqualini, F.S., Agarwal, A., Yuan, H., Jiang, D., Zhang, D., Zangi, L., et al. (2014). Modeling the mitochondrial cardiomyopathy of Barth syndrome with induced pluripotent stem cell and heart-on-chip technologies. Nat. Med. *20*, 616–623.
48. Wang, T., Birsoy, K., Hughes, N.W., Krupczak, K.M., Post, Y., Wei, J.J., Lander, E.S., and Sabatini, D.M. (2015). Identification and characterization of essential genes in the human genome. Science *350*, 1096–1101.
49. Pemble, H., Kumar, P., van Haren, J., and Wittmann, T. (2017). GSK3-mediated CLASP2 phosphorylation modulates kinetochore dynamics. J. Cell Sci. *130*, 1404–1412.
50. Le Berre, M., Aubertin, J., and Piel, M. (2012). Fine control of nuclear confinement identifies a threshold deformation leading to lamina rupture and induction of specific genes. Integr. Biol. *4*, 1406–1414.
51. Kuhl, F.P., and Giardina, C.R. (1982). Elliptic Fourier features of a closed contour. Comput Vision Graph *18*, 236–258.
52. Diaz, G., Quacci, D., and Dell'Orbo, C. (1990). Recognition of cell surface modulation by elliptic Fourier analysis. Comput. Methods Programs Biomed. *31*, 57–62.
53. Neto, J.C., Meyer, G.E., Jones, D.D., and Samal, A.K. (2006). Plant species identification using Elliptic Fourier leaf shape analysis. Comput. Electron. Agric. *50*, 121–134.
54. Sánchez-Corrales, Y.E., Hartley, M., van Rooij, J., Marée, A.F.M., and Grieneisen, V.A. (2018). Morphometrics of complex cell shapes: Lobe contribution elliptic Fourier analysis (LOCO-EFA). Development *145*, 145.
55. Mattes, D.H., Haynor, D.R., Vesselle, H., Lewellen, T.K., and Eubank, W. (2001). Nonrigid multimodality image registration. Proc. SPIE 4322, Medical Imaging 2001: Image Processing.
56. Cetera, M., Ramirez-San Juan, G.R., Oakes, P.W., Lewellyn, L., Fairchild, M.J., Tanentzapf, G., Gardel, M.L., and Horne-Badovinac, S. (2014). Epithelial rotation promotes the global alignment of contractile actin bundles during Drosophila egg chamber elongation. Nat. Commun. *5*, 5511.
57. Seara, D.S.L., Linsmeier, I., Tabatabai, P., Oakes, P.W., Tabei, S.M.A., Banerjee, S., and Murrell, M.P. (2018). Filament bending promotes dynamic stability in unconventional soft active nematics. arXiv, arXiv: 1804.04232 [cond-mat.soft]. https://arxiv.org/abs/1804.04232.

STAR★METHODS

KEY RESOURCES TABLE

REAGENT or RESOURCE	SOURCE	IDENTIFIER
Antibodies		
Mouse anti-α-tubulin conjugated to AF488	Cell Signaling	Cat# 8058S
Rabbit anti-α-tubulin	Sigma	Cat# T3526; RRID:AB_261659
Mouse anti-α-tubulin	Sigma	Cat# T6199; RRID:AB_477583
Rabbit anti-NuMA	Novus Biologicals	Cat# NB500-174; RRID:AB_10002562
Mouse anti-dynein intermediate chain	Millipore	Cat# MAB1618MI; RRID:AB_2246059
Rabbit anti-γ-tubulin	Sigma	Cat#T3559; RRID:AB_477575
Mouse anti-centrin	Millipore	Cat# 04-1624; RRID:AB_10563501
Alexa 488 goat anti-mouse IgG	Thermo Fisher	Cat# A11001; RRID:AB_2534069
Alexa 488 goat anti-rabbit IgG	Thermo Fisher	Cat# A11008; RRID:AB_143165
Alexa 568 goat anti-mouse IgG	Thermo Fisher	Cat# A11004; RRID:AB_2534072
Alexa 568 goat anti-rabbit IgG	Thermo Fisher	Cat# A11011; RRID:AB_143157
Alexa 647 goat anti-mouse IgG	Thermo Fisher	Cat# A21236; RRID:AB_2535805
Alexa 647 goat anti-rabbit IgG	Thermo Fisher	Cat# A21244; RRID:AB_2535812
Chemicals, Peptides, and Recombinant Proteins		
STLC	Sigma	Cat# 164739
MG132	Millipore	Cat# 474790
R0-3306	Sigma	Cat# SML0569
SiR-tubulin dye	Cytoskeleton, Inc.	Cat# CYSC-002
Verapamil	Cytoskeleton, Inc.	Cat# CYSC-002
MitoTracker Red	Sigma	Cat# M7512
Hoechst 33342	Sigma	Cat# H3570
Experimental Models: Cell Lines		
Human: RPE1 inducible NuMA knockout cells expressing GFP-tubulin	This paper	n/a
Human: RPE1 inducible dynein heavy chain knockout cells expressing GFP-tubulin	This paper	n/a
Human: RPE1 inducible NuMA knockout cells	[23]	n/a
Human: RPE1 inducible dynein heavy chain knockout cells	[42]	n/a
Oligonucleotides		
sgRNA #2 targeting human NuMA: 5′-AAGTCCAGTCTCTC TGACAC-3′	[23]	n/a
sgRNA #D2.1 targeting human dynein heavy chain: 5′-CAC CGCAGAATGTGGCGGACGTGT-3′	[42]	RPE line #D2.1 http://cellcycleknockouts.wi.mit.edu/
Software and Algorithms		
MATLAB	MathWorks	R2013B
PIVlab	[43], [44]	1.41
Fiji	ImageJ	2.0.0-rc-54
Trackmate	[45]	3.4.2
Metamorph	MDS Analytical Technologies	7.7.8.0
Other		
35 mm MatTek Dishes (poly-D-lysine coated)	MatTek Corporation	Cat# P35GC-1.5-20-C

CONTACT FOR REAGENT AND RESOURCE SHARING

Further information and requests for resources and reagents should be directed to and will be fulfilled by the Lead Contact, Sophie Dumont (sophie.dumont@ucsf.edu).

EXPERIMENTAL MODEL AND SUBJECT DETAILS

RPE1 cells (female human retinal epithelial cells) were cultured at 37°C and 5% CO_2 in DMEM/F12 (11320; Thermo Fisher) supplemented with penicillin/streptomycin and 10% tetracycline-screened FBS (SH30070.03T; Hyclone Labs, Logan, UT). Cells tested negative for mycoplasma. To generate inducible CRISPR NuMA knockout cells [23], we used a RPE1 cell line containing doxycycline-inducible human codon-optimized spCas9 that was a gift from I. Cheeseman (Whitehead/MIT) and was generated as described in [46] using a derivative of the transposon described in [47]. We designed sgRNAs against 5′ exons of NuMA using http://crispr.mit.edu and cloned them into the pLenti-sgRNA plasmid (gift from T. Wang, D. Sabatini, and E. Lander, Whitehead/Broad/MIT) under control of the hU6 promoter. We infected this inducible-spCas9 RPE1 cell line with each pLenti-sgRNA as described in [48] using virus expressed in HEK293T cells and 10 μg/mL polybrene and selected with 6 μg/mL puromycin. We tested three independent sgRNA sequences, each of which generated indistinguishable spindle phenotypes (data not shown), and picked one line for subsequent studies. Inducible CRISPR dynein (dynein heavy chain; DHC) knockout cells were a generous gift from I. Cheeseman (Whitehead/MIT) and published in [42]. Subsequently, to generate cell lines stably expressing GFP-tubulin, inducible NuMA and dynein knockout cells were infected with GFP-tubulin lentivirus and selected with 2.5 μg/mL blasticidin. Virus was made in HEK293T cells from a pLenti6/V5-DEST plasmid (Invitrogen) containing GFP-tubulin (gift of T. Wittmann [49]). Four days before each experiment, spCas9 expression was induced with 1 μM doxycycline hyclate.

METHOD DETAILS

Live cell imaging

Cell lines used have CRISPR/spCas9 and sgRNA stably integrated, but spCas9 expression is only induced upon doxycycline addition before each experiment, allowing for genetic manipulation of essential mitotic genes. For imaging, cells were plated on 35 mm #1.5 coverslip glass-bottomed dishes coated with poly-D-lysine (MatTek) and imaged in a stage-top humidified incubation chamber (Tokai Hit, Fujinomiya-shi, Japan) maintained at 30°C and 5% CO_2. To label mitochondria, 25 nM MitoTracker Red (Sigma) was added to cell media for 30 min and washed out before imaging. For some experiments, 100 nM siR-tubulin dye (Cytoskeleton, Inc.) was added 2 h prior to imaging to label microtubules, along with 10 μM verapamil (Cytoskeleton, Inc.). Under these conditions, there was no detected defect in spindle appearance or microtubule dynamics. As described in [21], cells were imaged using an Eclipse Ti-E inverted microscope (Nikon Instruments) with a Yokogawa CSU-X1 spinning disk confocal operated by MetaMorph (7.7.8.0; Molecular Devices), with either a 100X 1.45 Ph3 oil objective (Figure 3), a 60X 1.4 Ph3 oil objective (Figures 1 and 2), or a 20X 0.5 Ph1 air objective (Figure 4), and with an Andor iXon3 camera.

Immunofluorescence and antibodies

For immunofluorescence, cells were plated on #1.5 25 mm coverslips coated with 1 mg/mL poly-L-lysine. Cells were fixed with 95% methanol + 5 mM EGTA at −20°C for 3 min, washed with TBS-T (0.1% Triton X-100 in Tris-buffered saline), and blocked with 2% BSA in TBS-T for 1 h. Primary and secondary antibodies were diluted in TBS-T + 2% BSA and incubated with cells overnight at 4°C (primary) or for 20 min at room temperature (secondary). DNA was labeled with Hoescht 33342 (Sigma) before cells were mounted in ProLongGold Antifade (Thermo Fisher). Cells were imaged using the spinning disk confocal microscope described above. Antibodies: mouse anti-α-tubulin DM1α (T6199; Sigma), rabbit anti-α-tubulin (ab18251; Abcam, Cambridge, UK), rabbit anti-NuMA (NB500-174; Novus Biologicals), mouse anti-α-tubulin DM1α conjugated to Alexa488 (8058S; Cell Signaling), mouse anti-dynein intermediate chain (MAB1618MI; Millipore), rabbit anti-γ-tubulin (T3559; Sigma), and mouse anti-centrin (04-1624; Millipore).

Small molecule treatment

To inhibit Eg5 motor activity, we treated cells with 5 μM S-trityl-L-cysteine (STLC, Sigma). We resumed live cell imaging ~1 min after STLC addition. In Figure 2, time 00:00 indicates the first image after STLC addition. For experiments in Figures 1 and 2, control cells were held in metaphase for long-term imaging using 10 μM MG132, added 1 h before imaging. Because NuMA and dynein knockout cells already do not satisfy the spindle assembly checkpoint and are stuck in mitosis, MG132 addition was not necessary (and did not alter spindle morphology when added as a control). To synchronize mitotic entry for cell motility tracking (Figure 4), we treated cells overnight with 9 μM RO-3306 (Sigma) to synchronize them at the G2/M checkpoint. RO-3306 was washed out 50 min before imaging and replaced with standard media (or media + 10 μM MG132, for control cells).

Cell confinement

As in [37], cells were confined using a suction cup device adapted from a previous design [50] using soft-lithography techniques. SU8 was used to photolithographically pattern a negative relief of pillar structures (height 5 μm; diameter 200 μm; spacing 700 μm center to center). PDMS (Sylgard 184, Sigma) was mixed with curing agent and poured over the region at a 10:1 ratio. A 10-mm-diameter

coverslip was pressed onto the pattern and baked at 80°C for 1 h. The coverslip, with micropillar spacers attached, was attached to a suction cup device. For cell-confinement assays, the device was attached to a milliliter syringe, placed on a coverslip with adherent cells, and attached using negative pressure. Additional negative pressure was created by hand to lower the pillared coverslip onto cells. Approximately 30 min before imaging, confinement was applied gradually over a period of 5-10 min.

QUANTIFICATION AND STATISTICAL ANALYSIS

Quantification of spindle shape

Spindle long and short axis dimensions were measured using a home-written MATLAB (R2016a; The Mathworks, Inc.) program. Images of tubulin fluorescence (max intensity projections of a 2 μm z section) were passed through a median filter (3x3 pixels) and segmented using an intensity threshold. Spindle area (Figure 2C) was calculated based on the area (i.e., number of pixels) contained within the segmented region. For Figure 1C, an ellipse was fit to the segmented region, and the ellipse major axis length (spindle long axis) and minor axis length (spindle short axis) were measured and reported. To obtain spindle outlines, we used the perimeter of the segmented spindle region. To align spindle outlines over time and adjust for cell movement, we segmented cells (using a low tubulin intensity threshold) and calculated centroid position. We used these coordinates to align colored spindle outlines in Figures 1B and 2B.

Elliptical Fourier analysis of spindle shapes

Dynamic shape remodeling is one of the key features of knockout (KO) spindles that is much less pronounced in the wild-type (WT) variants. A quantitative demonstration of these differences is not a trivial task since the conventional morphological descriptors (e.g., the aspect ratio, area, etc.) do not accurately capture the complex variations in spindle shape. To enable a more informative comparison of spindle shapes, we employ the elliptical Fourier analysis method [51] which has been used extensively in morphological studies of biological shapes [52–54].

The workflow of the method is shown in Figures S1G–S1J, which is heavily based on the original implementation by Kuhl and Giardina [51]. First, the closed contour of the spindle (Figure S1G) is parametrized with a third "time" variable that stands for the position along the contour. This leads into two single-valued and periodic functions for the x-and y-projections (Figure S1H) and thereby makes them suitable for a Fourier analysis. The Fourier decompositions of the $x(t)$ and $y(t)$ projections are then obtained separately, resulting in

$$x_N(t) = A_0 + \sum_{n=1}^{N} a_n \cos\frac{2n\pi t}{T} + b_n \sin\frac{2n\pi t}{T},$$

$$y_N(t) = C_0 + \sum_{n=1}^{N} c_n \cos\frac{2n\pi t}{T} + d_n \sin\frac{2n\pi t}{T},$$

where A_0 and C_0 are offset constants, $\{a_n, b_n, c_n, d_n\}$ are the Fourier coefficients of the n^{th} harmonic, T is the length of the contour, and N is the total number of harmonics included in the Fourier decomposition. Each harmonic represents an ellipse that revolves n times around the first elliptic harmonic; hence, the name elliptical Fourier analysis. The reconstruction of the contour using its elliptical Fourier components can be obtained by plotting $x_N(t)$ and $y_N(t)$ back in the x-y plane. Figure S1I shows reconstructions where different numbers of harmonics were used. The $N = 1$ case includes only the first elliptic harmonic, which carries information about the approximate dimensions and the orientation of the contour. On the other hand, the reconstruction with $N = 10$ harmonics already captures the major variations in the spindle shape.

To quantify the contribution of each harmonic to shape variability, we follow the treatment by Diaz et al. [52] and introduce a mode strength metric defined as $P_n = n\sqrt{a_n^2 + b_n^2 + c_n^2 + d_n^2}$, where the square root term is proportional to the perimeter of the n^{th} harmonic ellipse which revolves n times around the first harmonic. Prior to calculating the mode strength spectrum for a contour, we normalize its size to have the major axis length of the first harmonic ellipse be unity [51], so that the comparison of different spindle contours reflects differences in their shapes and not the sizes. As an example, the mode strength spectrum corresponding to the contour in Figure S1G is depicted in Figure S1J. We note that since the mode spectrum $P_n(n = 1, \ldots, N)$ combines the information from individual coefficients $\{a_n, b_n, c_n, d_n\}$, it is not sufficiency to recover the original shape, but rather serves as a measure of shape complexity arising from different elliptical contributions.

Time correlation function of spindle shape

Using a home-written MATLAB program, spindles and cells were segmented as above. Binary images of segmented spindles were registered, allowing for both translation and rotation and optimizing image similarity using Mattes mutual information algorithm (MATLAB imregister) [55]. A mask based on cell segmentation was used to remove all pixels outside the cell from the subsequent correlation calculation. Then, a correlation coefficient (r) was calculated for pairs of registered binary images (image A at time t_1 and image B at t_2) using MATLAB's 2D correlation coefficient function, corr2:

$$r = \frac{\sum_m \sum_n (A_{mn} - \overline{A})(B_{mn} - \overline{B})}{\sqrt{\left(\sum_m \sum_n (A_{mn} - \overline{A})^2\right)\left(\sum_m \sum_n (B_{mn} - \overline{B})^2\right)}}$$

Conceptually, this shape correlation coefficient reports on the degree of spatial overlap between spindle shapes. As spindle shapes always overlap to some extent – the spindle never disappears – shape correlation generally ranges between ~0.7 – 0.9. To compute shape correlation as a function of lag time ($t_2 - t_1$), correlation coefficients were calculated and averaged for all possible pairs of video frames separated by a time interval of 4 min, then calculated and averaged for all pairs of frames separated by a time interval of 8 min, and so on. For each spindle, correlation coefficient (r) versus lag time data were fit by the exponential function $r = a * e^{(-1/\tau)*lag\ time} + b$ using MATLAB's curve fitting tool (see Figure S1K).

Nematic director field, order parameter, and correlation function

To obtain the nematic director field using a home-written MATLAB program, the spindle was first isolated in fluorescence images based on pixel intensity values, as shown in Figure S2A. Then, the image was divided into overlapping windows with dimensions of 15 × 15 px, with the window centers spaced 5 px apart on a grid (Figure S2B). Pixel information in each window was used to obtain the local director at the center via an established fast Fourier transform (FFT) method [56, 57], the workflow of which is as follows. First, a Gaussian filter was applied on the window to eliminate edge effects. Then, the 2-dimensional FFT was calculated, which is skewed in a direction that is perpendicular to the director. The principle skew direction was obtained by scanning over multiple lines with 1° resolution and choosing the direction θ_0 that maximizes the target function $L(\theta_0) = \sum_{ij} F_{ij} \left|\cos(\theta_{ij} - \theta_0)\right|$, where the summation is performed over all Fourier components with magnitudes F_{ij} and polar angles θ_{ij}. The rationale was to choose θ_0 that was closest to the angles of dominating Fourier components. The local director in real space was then identified as the direction perpendicular to the principal skew line (Figure S2C).

To estimate the degree of local alignment of microtubules, we calculated the local nematic order parameter at each grid position shown in Figure S2B via $s_{local} = 2(\langle \cos^2(\theta_i - \theta_0)\rangle - 0.5)$, where averaging was performed over the directors in a local domain defined by a 5 × 5 grid kernel (2 μm x 2 μm), and θ_0 was the angle corresponding to the nematic director of the domain that maximized $s_{local}(\theta_0)$ (Figure S2E) [57]. For locally disordered regions, we would expect the local nematic order parameter to be close to 0. Conversely, for locally aligned microtubules, the order parameter would be close to 1. A nematic order parameter field for a sample region of the NuMA KO spindle is shown in Figure S2F. We calculated the global nematic order parameter using $s_{global} = 2(\langle \cos^2(\theta_i - \theta_0)\rangle - 0.5)$, where the summation was now taken over all directors of the spindle, and θ_0 was chosen to maximize $s_{global}(\theta_0)$. The same θ_0 was used as the dominant orientation (Figure 2C), relative to which we calculated the distribution of director angles (Figure 2F).

Our calculation of the two-point correlation of nematic orientations $< \cos 2(\theta_r - \theta_0) >$ as a function of separation distance (Figure S2G) is illustrated in Figure S2H. For every possible pair of directors $\boldsymbol{n}_0$ and $\boldsymbol{n}_r$ within the spindle, we calculated $\cos 2(\theta_r - \theta_0)$ and binned by distance between 0 and r. Mean values for each bin were further averaged over all frames of a video. For a randomly oriented nematic director field, $< \cos 2(\theta_r - \theta_0) > = 0$. Similarly, the temporal nematic correlation of microtubule orientation (Figure 3G) was calculated using $< \cos 2(\theta_{t2} - \theta_{t1}) >$ as a function of lag time, t_2-t_1. (θ_{t1} is the angle of a given director at time t_1.) Correlations were calculated after translational registration of segmented spindle images by maximizing image cross-correlation (MATLAB's xcorr2 function).

Tracking aster dynamics

To obtain the trajectories of asters shown in Figure S2D, we first eliminated the bulk translational motion of the spindle caused by cell movement by registering the spindle segmentation masks relative to the first frame using a custom MATLAB program. Aster tracking was then done by finding the locations of intensity maxima in manually specified local regions near each aster at different time points.

Measuring intracellular flows and cell motility

To measure flows of tubulin and mitochondria during turbulent spindle rotations (Figure 4B), we used Particle Image Velocimetry tracking with MATLAB's PIVlab [43, 44]. Sequential PIV window sizes were 12.6, 6.3, and 4.2 μm. We used TrackMate software [45] on FIJI (ImageJ Version 2.0.0-rc-54) to track mitotic cell positions (Figure 4) using phase contrast images of cells imaged at 20X, from 1 h to 3 h after release into mitosis. Mean displacements and speeds (averaged over the 2 h window) were calculated in MATLAB. To correlate the spindle instability and cell displacement for individual NuMA knockout cells, we calculated the standard deviation (square root of the variance) of cell displacement and the square root of the circular variance (MATLAB's circular statistics toolbox [38]) of the orientation of the major spindle axis, a simple indicator of unstable microtubule organization, for individual cells over the 2 h window. We used Spearman's rank correlation coefficient (Spearman's rho) in MATLAB to calculate strength of association, since we do not assume a linear relationship.

Quantification of NuMA and dynein immunofluorescence

To measure NuMA and dynein intensity in control cells and cells in which NuMA or dynein heavy chain had been knocked out (Figures S1A and S1B), we used sum intensity projections of confocal immunofluorescence images, covering 7 μm in the z-dimension. Using a

home-written MATLAB program, cells were isolated using a low threshold for tubulin fluorescence intensity. We measured mean tubulin intensity and mean NuMA or dynein intermediate chain (DIC) intensity of sum intensity projections within the isolated cell region. We normalized NuMA or DIC intensity measurements for each cell by dividing by tubulin intensity.

Statistical analysis

Exponential decay fits were calculated in MATLAB. One-way ANOVA and Tukey post hoc tests (Figure 4D) and Spearman's rank correlations (Figure 4E) were performed in Microsoft Excel and MATLAB. Error bars and shaded regions throughout are standard error of the mean. Quoted n's are described in more detail in Figure Legends, but in general refer to individual spindles or cells.